



A numerical method for large-eddy simulation in complex geometries

K. Mahesh^{a,*}, G. Constantinescu^b, P. Moin^b

^a Department of Aerospace Engineering and Mechanics, University of Minnesota, Minneapolis, MN 55455, USA

^b Center for Turbulence Research, Stanford University, Stanford, CA 94305, USA

Received 22 July 2003; received in revised form 19 November 2003; accepted 19 November 2003

Available online 23 January 2004

Abstract

We discuss the development of a numerical algorithm, and solver capable of performing large-eddy simulation in the very complex geometries often encountered in industrial applications. The algorithm is developed for unstructured hybrid grids, is non-dissipative, yet robust at high Reynolds numbers on highly skewed grids. Simulation results for a variety of flows are presented.

© 2003 Elsevier Inc. All rights reserved.

Keywords: Large-eddy simulation; Unstructured grids; Complex geometries; Energy-conserving schemes; Gas-turbine combustor

1. Introduction

The Navier–Stokes and continuity equations for incompressible flow are

$$\frac{\partial u_i}{\partial t} + \frac{\partial u_i u_j}{\partial x_j} = -\frac{\partial p}{\partial x_i} + \nu \frac{\partial^2 u_i}{\partial x_j \partial x_j}, \quad \frac{\partial u_i}{\partial x_i} = 0. \quad (1)$$

Note that the density is assumed constant, and absorbed in the pressure throughout this paper. Large-eddy simulation (LES) is an unsteady, three-dimensional simulation methodology where the Navier–Stokes equations are spatially filtered, the resolved scales of motion are directly computed, and the influence of the filtered scales on the resolved scales is modeled. Spatial filtering (denoted by the overbar) of the Navier–Stokes equations with a filter that commutes with the spatial and temporal derivatives yields the LES equation

$$\frac{\partial \bar{u}_i}{\partial t} + \frac{\partial \bar{u}_i \bar{u}_j}{\partial x_j} = -\frac{\partial \bar{p}}{\partial x_i} + \nu \frac{\partial^2 \bar{u}_i}{\partial x_j \partial x_j} + \frac{\partial \tau_{ij}}{\partial x_j}, \quad \frac{\partial \bar{u}_i}{\partial x_i} = 0. \quad (2)$$

Here, $\tau_{ij} = \bar{u}_i u_j - \bar{u}_i \bar{u}_j$ is the subgrid stress, and is modeled.

* Corresponding author.

E-mail address: mahesh@aem.umn.edu (K. Mahesh).

LES and direct numerical simulation (DNS) have largely been used to study turbulent flows in simple configurations [27]. The primary reason for this is computational cost. Prediction of engineering flows relies on the Reynolds-averaged Navier–Stokes equations (RANS), where turbulence models for $\langle u'_i u'_j \rangle$ allow the time-averaged or ensemble-averaged solution to be directly obtained (the brackets $\langle \rangle$ denote the average, and the primes denote fluctuations about the average). However, there is increasing interest in applying LES to complex problems because of its greater accuracy over RANS, particularly for phenomena such as turbulent mixing and aerodynamic noise. Unfortunately, the numerical methods used to solve the RANS equations are not directly applicable to LES. RANS typically uses upwinded numerical methods which provide numerical dissipation and make the solution procedure robust. When used for LES, upwinding compromises accuracy (e.g. [24]) since the numerical dissipation competes with, and often overwhelms the effect of the subgrid model and molecular viscosity.

By definition, the dissipative scales are not resolved by the grid in LES. In practice, this leads to numerical instability if straight-forward, non-dissipative central-difference schemes are used. The instability is related to aliasing errors that occur when non-linear products are computed in physical space (see, e.g. [25]). One solution to this problem is to develop non-dissipative numerical schemes that discretely conserve not only first-order quantities such as momentum, but also second-order quantities such as kinetic energy (e.g. [2,4,14,22]). Discrete energy conservation ensures that the flux of kinetic energy, $\sum_{\text{cvs}} u_i \partial(u_i u_j) / \partial x_j$ only has contributions from the boundary elements (the summation is over all the control volumes of the mesh). This makes the solution robust without the use of numerical dissipation. Note that satisfying one constraint discretely, does not ensure the other – both constraints have to be simultaneously enforced when deriving the algorithm. The Harlow–Welch algorithm [8] possesses this property on *structured* grids, and has therefore been widely used for LES on structured grids in simple geometries.

There is considerable incentive to develop LES on unstructured grids. In addition to reducing the number of mesh nodes, unstructured grids significantly reduce the amount of time spent on grid generation. Although a variety of numerical methods exist to compute flows on unstructured grids (see, e.g. [3]), their application to LES is scarce. Most methods have been developed either for laminar flow or for the steady RANS equations. An exception is the work of [11] who performed LES of high Reynolds number flow past the NACA 4412 airfoil using the Galerkin/least-squares finite element method [9].

Not much attention has been paid to discrete energy conservation on unstructured grids. Exceptions are Perot [31] and Zhang et al. [34] who discuss discrete energy-conservation for staggered schemes on triangular or tetrahedral unstructured grids. Also discussed are the roles of discrete operators for the curl and divergence in ensuring kinetic energy conservation. Such operators for unstructured quadrilateral meshes are also discussed by Hyman and Shashkov [10], who term them “mimetic schemes”. Related work is that by Amit et al. [1] who use the notion of dual or co-volumes to develop a staggered algorithm for two-dimensional triangular grids. A similar formulation is developed and analyzed in detail by Nicolaides [28] and Nicolaides and Wu [29] for the divergence–curl, and Navier–Stokes equations in two and three dimensions. A collocated, implicit formulation is developed by Kim and Choi (2002) and applied to laminar, two-dimensional flow on hybrid unstructured grids.

None of the above finite-volume formulations have been applied to DNS or LES. This paper develops a finite-volume algorithm for LES on unstructured grids with arbitrary elements. The formulation is non-dissipative; yet robust and accurate at high Reynolds numbers on highly distorted grids. Discrete energy-conservation was found to be extremely important in ensuring this behavior. Detailed validation studies are presented for a wide variety of flows – Taylor problem, isotropic turbulence, flow over a circular cylinder and the flow in a coaxial combustor. Also shown are results from simulations in the exceedingly complex geometry of a commercial gas-turbine engine combustor.

The paper is organized as follows. Section 2 generalizes the Harlow–Welch formulation to unstructured grids using a rotational form of the convection terms. While elegant, this formulation is found lacking when

extended to three-dimensions. In particular its restriction to tetrahedral elements, and lack of robustness on skewed grids are serious practical limitations. An alternative formulation is therefore derived in Section 3 for use on arbitrary elements. Section 3.2 discusses simulation results for a variety of flows to show that robust, accurate solutions are now obtained at high Reynolds numbers in very complex geometries on highly skewed grids. The paper concludes with a brief summary in Section 4.

2. Staggered rotational formulation

The popular staggered formulation by Harlow and Welch [8] on structured grids is extended to unstructured grids of triangles in two-dimensions and tetrahedra in three dimensions as follows. Fig. 1 shows a single triangular element. Note that the pressure is stored at the circumcenter of the element (the intersection of the perpendicular bisectors of the edges), while the velocities normal to the edges of the triangle are stored at the edge-centers.

Analogous to the procedure on a structured grid, the velocity components normal to the edges are time-advanced using the governing equations, while the components tangential to the edges are obtained by interpolating the velocities normal to the other edges. Consider an edge. Denote the normal to the edge by \vec{n} . In two dimensions, there are two volumes that straddle each edge, and are denoted by the indices 1 and 2, respectively. Likewise, the two nodes of each edge are assigned the indices 1 and 2. The edge-normal is defined so that it points from volume 1 to volume 2, and the tangent to the edges is defined such that it points from node 1 to node 2.

The normal velocity component v_n is equal to $\vec{u} \cdot \vec{n}$. The dot product of the Navier–Stokes equations (Eq. (1)) with \vec{n} yields the governing equation for v_n ; i.e.,

$$\frac{\partial v_n}{\partial t} - (\vec{u} \times \vec{\omega}) \cdot \vec{n} + \frac{\partial}{\partial n} \left(\frac{\vec{u} \cdot \vec{u}}{2} \right) = -\frac{1}{\rho} \frac{\partial p}{\partial n} + \nu (\nabla^2 \vec{u}) \cdot \vec{n}, \tag{3}$$

where, $\vec{\omega} = \nabla \times \vec{u}$ denotes the vorticity. It is easily seen that in 2D,

$$(\vec{u} \times \vec{\omega}) \cdot \vec{n} = \omega v_t, \tag{4}$$

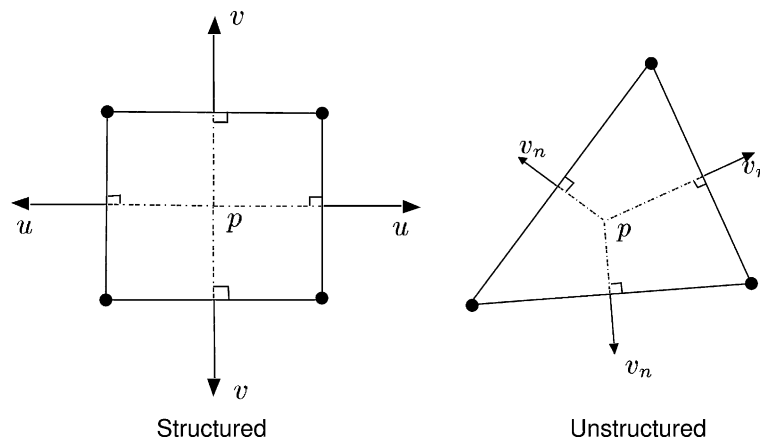


Fig. 1. The staggered positioning of variables on an unstructured mesh of triangles is contrasted with that on a structured mesh.

where v_t denotes the tangential velocity component. Consider next the viscous term. We have the vector identity,

$$\nabla^2 \vec{u} = -\nabla \times \vec{\omega} + \nabla (\nabla \cdot \vec{u}). \tag{5}$$

If the velocity field is divergence-free, this implies in 2D that

$$(\nabla^2 \vec{u}) \cdot \vec{n} = -\frac{\partial \omega}{\partial s_t}, \tag{6}$$

where s_t denotes the tangential derivative along the edge. To time-advance the momentum equation, we therefore need the vorticity at the nodes and the edge-centers, tangential velocity at edge centers, total kinetic energy and pressure at the cell-centers.

The vorticity at the nodes (or more generally the curl of a vector whose edge-normal component is known) is computed using Green’s theorem, i.e.,

$$\int_A \omega dA = \int_C \vec{u} \cdot d\vec{l}. \tag{7}$$

The area over which the integration is performed (A_{dual}) is shown in Fig. 2, and is obtained by joining the circumcenters of the triangles that surround the node. The dashed lines indicate the boundaries of this area. It is easily seen that the velocity components parallel to the edges of this area are normal to the edges of the triangles that make up the area. The vorticity at the node ‘ n ’ is therefore computed as

$$\omega = \frac{1}{A_{\text{dual}}} \sum_e v_{ne} l_d, \tag{8}$$

where l_d is the distance between the circumcenters of the triangles that constitute the dual mesh (see Fig. 2).

This procedure is easily applied in an edge-based data structure, where the volumes and nodes that straddle each edge are stored. The nodal vorticities may therefore be calculated by looping over the edges, evaluating the distance between the circumcenters of the neighboring volumes, computing the product of the normal velocity and the distance between circumcenters and adding the product to one of the nodes of the edge, and subtracting it from the other. Once the nodal vorticities are known, the vorticity at the edge-centers may be computed as the average of the vorticity at the corresponding nodes. Also the tangential derivative of the vorticity at the edge-center may be computed as the difference of the nodal vorticities divided by the edge length. These approximations are second-order accurate in the edge length.

Analogous to the staggered-grid approach on structured grids, the tangential velocities on edge-centers are obtained by interpolating from the normal velocities on the surrounding edges. This process is fairly

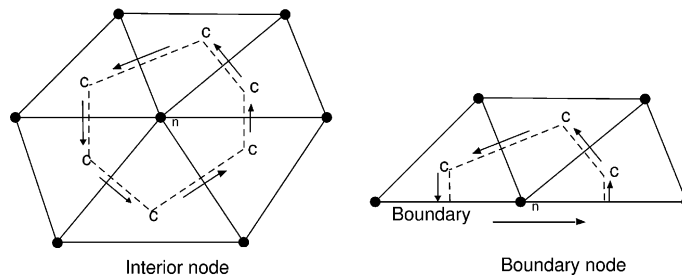


Fig. 2. Illustration of the dual mesh used to compute the vorticity at the nodes.

simple on structured grids where the coordinate directions are generally orthogonal in physical or computational space. However obtaining the tangential velocities on unstructured grids requires solving a system of equations. The interpolation is performed as follows. Referring to Fig. 3, the velocity tangential to each edge v_t is unknown, while the normal velocity is known. Project the velocity vectors on the four neighboring edges along the direction of the central edge. The tangential velocity at the central edge is then expressed as the weighted average of the projected velocities at the neighboring four edges. This yields the elements of the coefficient matrix $A[v_i] = [b]$ where the projected edge-normal velocities make up the right-hand side vector b . In the current implementation, we use a first-order approximation on a non-uniform grid, second-order on an uniform grid; i.e., the tangential velocity at the central edge is the average of the projected velocity vector at the neighboring four edges.

A fractional step approach for the pressure is derived. A direct analogy with the structured grid algorithm may be drawn. The algorithm ensures that as the solution is advanced from time t_k to t_{k+1} , the divergence of the velocity field at t_{k+1} is machine zero (or proportional to the level to which the pressure equation is converged). Denote the nonlinear terms in Eq. (3) by NL and the viscous terms by VISC, and use the Adams–Bashforth method for time integration for both. Neglecting the pressure in the first fractional step, we have

$$\frac{\widehat{v}_n - v_n^k}{\Delta t} = \frac{1}{2} [3(\text{NL} + \text{VISC})^k - (\text{NL} + \text{VISC})^{k-1}], \tag{9a}$$

$$\frac{v_n^{k+1} - \widehat{v}_n}{\Delta t} = -\frac{\partial p^{k+1}}{\partial n}. \tag{9b}$$

We require that the divergence of the velocity field at t_{k+1} be zero. Application of the divergence theorem to each element yields

$$V \nabla \cdot \vec{u} = \sum_e v_{ne} l_e, \tag{10}$$

where V is the element volume (area of the triangle in 2D), v_{ne} is the normal velocity component associated with an edge and l_e is the length of the edge of the 2D element. Eq. (9b) holds for each edge. Consider the three edges that bound a volume. For each edge of the volume, multiply Eq. (9b) by the edge-length, and add the product for all three edges. This yields

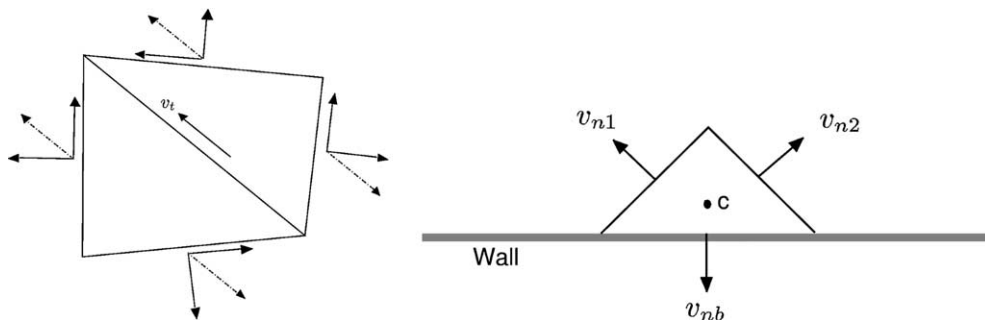


Fig. 3. (a) Illustration of the interpolation stencil for the tangential velocity at the edges. (b) Schematic of a boundary volume. The solid vectors are the normal and tangential velocities on the edges, while the dashed line denotes projection of the velocity vector along the edge under consideration.

$$\frac{1}{\Delta t} \sum_{\mathbf{e}} v_{\text{ne}}^{k+1} l_{\mathbf{e}} - \frac{1}{\Delta t} \sum_{\mathbf{e}} \widehat{v}_{\text{ne}} l_{\mathbf{e}} = - \sum_{\mathbf{e}} \frac{\partial p^{k+1}}{\partial n} l_{\mathbf{e}}. \quad (11)$$

Using Eq. (10) for the divergence and the continuity equation written at time t_{k+1} , we require that $\sum_{\mathbf{e}} v_{\text{ne}}^{k+1} l_{\mathbf{e}} = 0$. This requires that the pressure satisfy

$$\sum_{\mathbf{e}} \frac{\partial p^{k+1}}{\partial n} l_{\mathbf{e}} = \frac{1}{\Delta t} \sum_{\mathbf{e}} \widehat{v}_{\text{ne}} l_{\mathbf{e}}. \quad (12)$$

Since p is stored at the circumcenter of the volume, its gradient normal to the edge is easily computed. This yields a set of discrete equations for p that are then solved. These discrete equations are of the form,

$$c(i)p(i) + \sum_{j=1}^3 c(i,j)p(j) = \text{rhs}(i), \quad (13)$$

where the sum over j is a sum over the three (triangles) volumes that are neighbors of volume ' i '. Eq. (13) is easily written for the interior volumes. When it is applied to a boundary volume, it appears that the gradient of p at the boundary is required. However this is not the case (see e.g. [26]); this requirement can be circumvented as follows. Fig. 3 shows a boundary element. Assume that Dirichlet boundary conditions on the velocity are specified at the boundary. The divergence-free condition requires that

$$\sum_{\mathbf{e}} v_{\text{ne}} l_{\mathbf{e}} = 0; \quad \text{i.e.,} \quad \sum_{\text{interior edges}} v_{\text{ne}} l_{\mathbf{e}} = -v_{\text{nb}} l_{\text{eb}}, \quad (14)$$

where the subscript b refers to the boundary edges. This implies that the pressure equation for the boundary elements may be obtained by summing Eq. (12) over the interior edges alone, and using Eq. (14) to relate the interior sum of the velocity to the normal velocity at the boundary; i.e.,

$$\sum_{\text{interior edges}} \frac{\partial p^{k+1}}{\partial n} l_{\mathbf{e}} = \frac{1}{\Delta t} \sum_{\text{interior edges}} \widehat{v}_{\mathbf{e}} l_{\mathbf{e}} + \frac{1}{\Delta t} v_{\text{nb}} l_{\text{eb}}. \quad (15)$$

This eliminates the need for boundary conditions on p .

2.1. Validation

2.1.1. Laminar flow in a driven cavity

Results are presented for the steady laminar flow in a two-dimensional driven cavity at a Reynolds number of 5000 (Fig. 4). Results from the structured grid computations by Ghia et al. [6] are used for validation. The quantities validated include velocity and vorticity profiles (Fig. 5). The unstructured grid allows fewer points to be used. Table 1 lists some details of the grids used. Corresponding details of Ghia et al.'s computations are also shown. No attempt was made to optimize the unstructured grids; good agreement with the structured grid results is seen (Fig. 5).

2.1.2. Unsteady evaluation

The Taylor problem has the following analytical solution to the Navier–Stokes equations (on a domain of unit size in both directions):

$$u = -\cos 2\pi x \sin 2\pi y e^{-8\pi^2 t}, \quad v = \sin 2\pi x \cos 2\pi y e^{-8\pi^2 t} \quad (16)$$

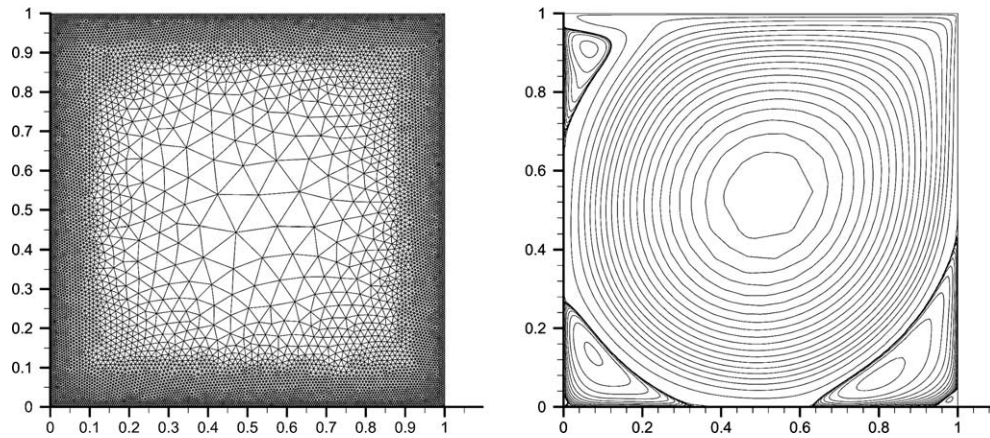


Fig. 4. Grid and contours of the streamfunction in driven cavity simulations at $Re = 5000$.

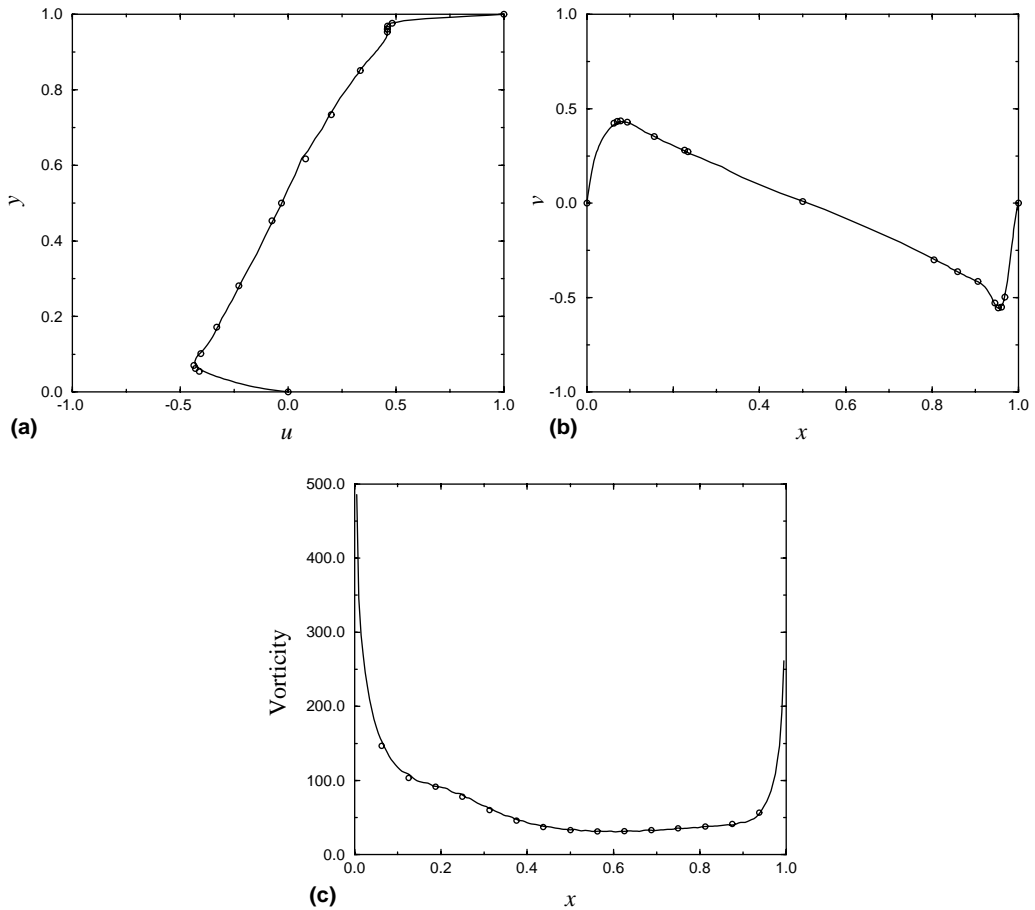


Fig. 5. Unstructured results (solid lines) are compared to results from Ghia et al. (symbols) for the flow in a driven cavity. The Reynolds number is 5000. (a) Vertical profile of streamwise velocity at $x = 0.5$. (b) Streamwise profile of vertical velocity at $y = 0.5$ (c) vorticity at the top boundary.

Table 1

Comparison of the grid used in the unstructured computations to the structured grid used by [6] in driven cavity simulations

	Unstructured	Structured
Nodes	10576	66049
Elements	30925	65536
Δ_{\min}	0.005	0.004
Δ_{\max}	0.1	0.004

Δ_{\min} and Δ_{\max} denote the minimum and maximum edge-lengths, respectively.

and is used for unsteady flow validation. Note that the Taylor problem corresponds to periodic, counter-rotating vortices whose strength decays in time at a rate determined by the viscosity. Fig. 6 shows the decay in kinetic energy as a function of time. The mesh has an edge-length of 0.05, and the CFL number is 1. The computation was run long enough that the kinetic energy decayed by a factor of 50. Note that the error at the end of the first time-step is slightly larger ($\sim 1\%$) than that at the subsequent substeps. The explicit Euler scheme is used at the first timestep, while subsequent substeps use the second-order Adams–Bashforth method. The lower accuracy of the explicit Euler was thought responsible for this behavior. However, time-step refinement at the first substep showed no change in the error. This raised some concern if the time-advancement at the first substep was zeroth-order, and if the fractional step approach for pressure was responsible. The fractional step approach was therefore replaced by the straightforward explicit Euler at the first timestep. Pressure was obtained by solving the Poisson equation obtained from the divergence of the nonlinear and viscous terms. The error still persisted. It turns out that source of the error is the the interpolation of v_n to obtain v_t . The first time-step is different from subsequent timesteps in that v_n is obtained from the analytical solution, and v_t is immediately obtained by interpolation. Subsequent time-steps consistently obtain both components from the projection step and interpolation, respectively. This was verified by replacing the interpolated value for v_t by the exact value; the error was eliminated. Structured staggered-schemes will have similar error.

A grid convergence study was performed to verify that the overall spatial discretization is second-order. The edge-lengths were progressively refined from 0.1 to 0.0125 in factors of 2. A fixed CFL number of 1 was used to run the flow out to a dimensional time of 0.025. This corresponds to a non-dimensional time ($8\pi^2 t$) of 2. The kinetic energy decays by a factor of approximately 50 over this time. The fractional error,

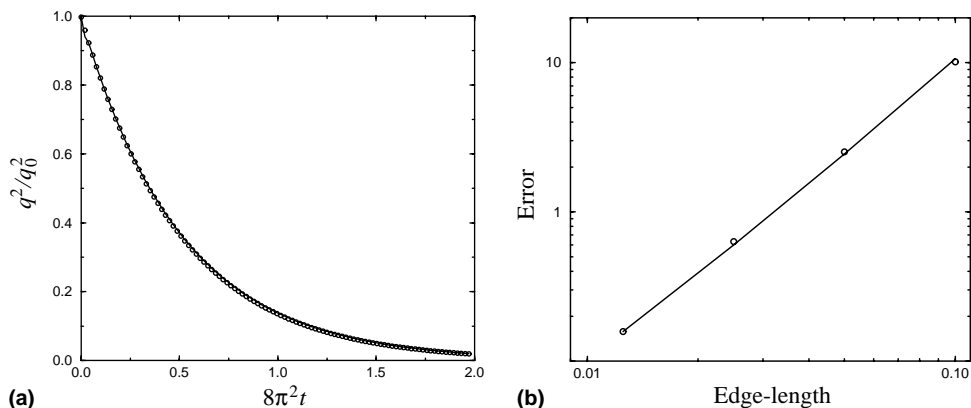


Fig. 6. (a) The decay of kinetic energy from the unstructured algorithm (solid line) is compared to the analytical solution (symbols) for the Taylor problem. The edge-length is 0.05 and the CFL number is 1. (b) The percentage error in kinetic energy as a function of resolution. The solid line corresponds to a second-order accurate scheme while the symbols are from the computation.

$100(q_{\text{computed}}^2/q_{\text{exact}}^2 - 1)$ at the end of the run is shown in Fig. 6. The error in kinetic energy is seen to drop by a factor of 4 every time the mesh is refined, confirming that the spatial discretization is indeed second-order.

2.2. Extension to three-dimensions

The algorithm is extended to tetrahedral elements as follows. Fig. 7 shows a tetrahedral element. Each element is comprised of four nodes, four faces and five edges. The pressure and any scalars are stored at the circumcenter of the tetrahedron. The velocity component normal to each face, v_n is stored at the circumcenter of each face. The correspondence to the classical staggered positioning of variables on structured grids is apparent. The usual structured grid algorithm may be interpreted in an unstructured manner as follows. On each face one solves for the face-normal velocity. Tangential velocity components, when needed on the face are obtained by interpolating the velocities from the surrounding faces. Defining pressure at the cell-centers, allows pressure gradients at the faces to be computed in a natural manner

$$\left(\frac{\partial p}{\partial n}\right)_{\text{face}} = \frac{(p_{\text{cv2}} - p_{\text{cv1}})}{d_f}, \tag{17}$$

where cv1 and cv2 are the two cells having that particular face in common, d_f is the distance between the circumcenters of cv1 and cv2 and n is the face-normal pointing from cv1 to cv2. Also, solving for the face-normal velocities allows the discrete divergence at the cell-centers to be computed using the divergence theorem, which in turn allows the pressure in a pressure-projection approach to be consistent with the discrete continuity equation. This interpretation forms the basis of the unstructured algorithm. The only caveat is that the convection term has to be computed in velocity–vorticity (rotational) form.

Consider the term $(\vec{u} \times \vec{\omega}) \cdot \vec{n}$ in Eq. (3). Decompose the velocity and vorticity into components parallel and perpendicular to \vec{n} ; i.e.,

$$\vec{u} = v_n \cdot \vec{n} + \vec{v}_t, \quad \vec{\omega} = \omega_n \cdot \vec{n} + \vec{\omega}_t. \tag{18}$$

Since \vec{n} is normal to a face, the tangential components lie in the plane of the face. The vector identities,

$$\vec{a} \cdot (\vec{b} \times \vec{c}) = \vec{b} \cdot (\vec{c} \times \vec{a}) = \vec{c} \cdot (\vec{a} \times \vec{b}) \tag{19}$$

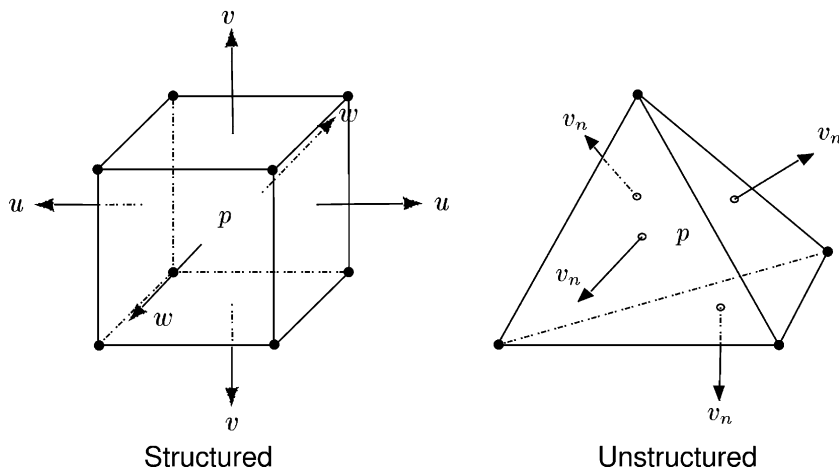


Fig. 7. The staggered positioning of variables on an unstructured mesh of tetrahedra.

may be used to show that only the components of velocity and vorticity that lie in the plane of the face contribute to $(\vec{u} \times \vec{\omega}) \cdot \vec{n}$; i.e.,

$$(\vec{u} \times \vec{\omega}) \cdot \vec{n} = \vec{v}_t \cdot (\vec{\omega}_t \times \vec{n}). \quad (20)$$

The tangential velocity components are obtained as follows. Each face has three edges. On each face arbitrarily define two basis vectors that are aligned with edges 1 and 2. These two basis vectors define the two tangential directions on the face. Denote the velocity components along these directions as v_{t1} and v_{t2} ($\vec{v}_t = v_{t1} \cdot \vec{i}_1 + v_{t2} \cdot \vec{i}_2$). Analogous to the two-dimensional algorithm, a set of equations is derived for the tangential velocity components by interpolating the velocities from the neighboring faces.

There are two steps to obtaining the vorticity components in the plane of each face. First, the circulation theorem is invoked to obtain the vorticity along each edge of the face. The circulation theorem is applied on a closed circuit around each edge. This circuit is obtained by joining the circumcenters of the tetrahedra of which this edge is part. This is made possible by the property of the circumcenter that all such segments will lie in the same plane. This is schematically shown in Fig. 8. Consider an edge along which we want the vorticity (the thick dashed line). Also shown are the faces that this edge is attached to. The circuit obtained by joining the circumcenters of the tetrahedra that straddle the faces is the thin dashed line. The circulation theorem,

$$A_{\text{dual}} \omega_e = \sum_{\text{dual edges}} v_{ne} l_d \quad (21)$$

is applied to this circuit to obtain the vorticity component along the edge. Note that the length of the edges of the dual mesh (l_d) is the distance between the circumcenters of the tetrahedra that constitute the dual mesh.

This process is easily performed in a face-based data structure. This vorticity is then projected along the tangential basis vectors on the face, and averaged to obtain $\vec{\omega}_t$ at the face circumcenter.

The viscous term is obtained from the edge-vorticities as follows. Consider the identity (5). If the velocity field is divergence-free, this implies that in 3D (analogous to Eq. (6) in 2D)

$$(\nabla^2 \vec{u}) \cdot \vec{n} = -(\vec{\nabla} \times \vec{\omega}) \cdot \vec{n}. \quad (22)$$

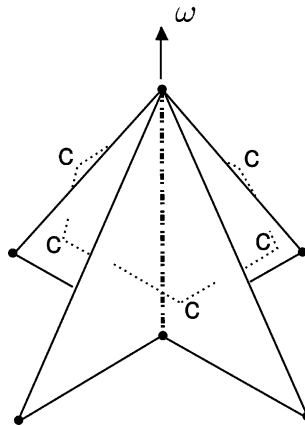


Fig. 8. Illustration of how the vorticity along each edge is computed.

Green's theorem shows that the curl of a vector along any direction may be related to the circulation of the vector on a circuit in a plane normal to that direction. This implies that the curl of the vorticity along the face-normal may be expressed in terms of its circulation along the face-edges; i.e.,

$$A_f (\vec{\nabla} \times \vec{\omega}) \cdot \vec{n} = \sum_e \omega_e l_e, \quad (23)$$

where ω_e is the vorticity component along the edges previously computed (see Eq. (21)), l_e denotes the edge-lengths of the face, and A_f denotes the area of the face.

2.3. Problems with formulation

While elegant, the above formulation has some limitations. It is restrictive in that pressure (and scalars if any) is stored at the circumcenter of the triangular elements. This restricts the grid to elements whose circumcenter lies within them. For example, in two-dimensions, consider right-triangles. Their circumcenter lies on the hypotenuse, making it impossible to determine the pressure gradient normal to the hypotenuse. Highly skewed elements are another source of problem since the circumcenter will now lie outside the element [17]. Although projection of the velocity field is still possible in this situation, the inaccurate computation of the pressure gradient is cause for concern. Skewed elements also render computation of the vorticity inaccurate.

A practical limitation concerns the restriction of the algorithm to tetrahedra. Although tetrahedra are well-suited to grid very complex geometries, experience shows that hexahedral elements are preferable since (i) hexahedral elements are more easily aligned with flow gradients such as boundary layers, and (ii) it takes fewer hexahedral elements to fill space than comparable tetrahedra. For example, a three-dimensional grid generated for an industrial (Section 3.3) gas-turbine combustor required a tetrahedral grid with approximately 600,000 nodes and 6.35 million faces (normal velocities to be solved) while a hexahedral grid with only 1.5 million nodes and faces yielded significantly higher resolution near the walls.

3. A non-staggered formulation

To address the problems of the staggered rotational formulation described above, an alternative approach was developed, and implemented for hybrid grids of tetrahedra, hexahedra, wedges and prisms. The basic idea is that the robustness at high Reynolds numbers is determined essentially by the numerical discretization of the convection term, while robustness on skewed grids is determined by both discretization of the convection and the pressure-gradient terms. For incompressible flows, discrete energy conservation refers to the fact that the convective and pressure terms in the discrete kinetic energy equation are expressible in divergence form. In contrast with the fully staggered approach outlined earlier, the Cartesian velocity components and pressure are stored at the centroids of the cells, while the face-normal velocities are treated as an independent variable which is stored at the centroids of the faces. Spatial discretization of the convective term is illustrated by the passive scalar equation,

$$\frac{\partial \phi}{\partial t} + \frac{\partial}{\partial x_i} \phi u_i = 0. \quad (24)$$

Note that $\partial u_i / \partial x_i = 0$ for incompressible flow. Multiplying by ϕ and using the continuity equation yields

$$\frac{\partial \phi^2}{\partial t} + \frac{\partial}{\partial x_i} \phi^2 u_i = 0, \quad (25)$$

i.e., conservation of ϕ implies conservation of ϕ^2 . However, discretely, conserving ϕ does not automatically imply conservation of ϕ^2 . Integrating Eq. (24) over a cell and using the divergence theorem yields

$$V_{cv} \frac{d\phi_{cv}}{dt} + \sum_{\text{faces of cv}} \phi_{\text{face}} v_n A_f = 0, \quad (26)$$

where ϕ_{cv} and V_{cv} denote the value of the scalar and the volume of cell ‘cv’, A_f is the face area, and v_n denotes the face-normal velocity in the direction of the outward normal at each face. Note that the incompressibility condition requires that $\sum_{\text{faces}} v_n A_f = 0$. Also, ϕ is discretely conserved regardless of how ϕ_{face} is computed. However, ϕ^2 will discretely be conserved only if the values of ϕ at the faces are calculated as a simple arithmetic mean of the values at the two cells that have that particular face in common; i.e.,

$$\phi_{\text{face}} = \frac{\phi_{cv} + \phi_{\text{nbr}}}{2}. \quad (27)$$

The discrete equation for ϕ^2 is obtained by multiplying Eq. (26) with ϕ_{cv} to obtain

$$V_{cv} \phi_{cv} \frac{d\phi_{cv}}{dt} + \frac{\phi_{cv}}{2} \sum_{\text{faces of cv}} (\phi_{cv} + \phi_{\text{nbr}}) v_n A_f = 0, \quad (28)$$

which may be rewritten as

$$\frac{V_{cv}}{2} \frac{d\phi_{cv}^2}{dt} + \frac{\phi_{cv}^2}{2} \underbrace{\sum_{\text{faces of cv}} v_n A_f}_{=0} + \frac{1}{2} \sum_{\text{faces of cv}} \phi_{cv} \phi_{\text{nbr}} v_n A_f = 0. \quad (29)$$

Summation over all the cells in the computational domain yields

$$\sum_{\text{volumes}} V_{cv} \frac{d\phi_{cv}^2}{dt} + \sum_{\text{volumes}} \sum_{\text{faces of cv}} \phi_{cv} \phi_{\text{nbr}} v_n A_f = 0. \quad (30)$$

The contribution from the interior faces cancel out in the second term to yield

$$\sum_{\text{volumes}} V_{cv} \frac{d\phi_{cv}^2}{dt} + \sum_{\text{boundary faces}} \phi_{cv} \phi_{\text{nbr}} v_n A_f = 0, \quad (31)$$

where if the boundary conditions for the scalar ϕ are specified on the boundary faces, one can define ϕ_{nbr} as $\phi_{\text{nbr}} = 2\phi_{\text{face}} - \phi_{cv}$. The above property is a statement of robustness since the summation of positive quantities is bounded.

Note that discrete energy-conservation is implied in the absence of time-discretization errors. Also, the discretization will have dispersive error to leading order, whose magnitude needs to be small to compute phenomena such as turbulent mixing of passive scalars. In our experience, in computations of turbulent flow fields, dissipative errors show up at the level of kinetic energy, while dispersive errors show up in higher order statistics. This motivates the choice of schemes that are non-dissipative, yet robust at high Reynolds numbers.

The interpolation, $\phi_{\text{face}} = (\phi_{cv} + \phi_{\text{nbr}})/2$ is second-order accurate on uniform grids. On non-uniform grids, the interpolant could be weighted by the distances between the faces and the neighboring volumes. However such weighted interpolation comes at the cost of not being discretely energy-conserving. Numerical examples show that on grids that vary rapidly, weighted interpolants can be unstable since the weights reflect the underlying grid roughness. The symmetric interpolation on the other hand is both en-

ergy-conserving and stable for arbitrarily non-uniform meshes, properties which are of prime importance for obtaining meaningful solutions in very complex geometries, where mesh irregularities cannot always be avoided.

The term $\phi_{cv}^2 \sum_{\text{faces of cv}} v_n A_f$ was dropped in Eq. (29) since $\sum_{\text{faces of cv}} v_n A_f$ is zero for incompressible flow. The Poisson equation for pressure enforces this incompressibility constraint. If the Poisson equation is solved using direct methods, then the discrete divergence will be zero to machine accuracy. However, it is more common to solve the Poisson equation iteratively; the discrete divergence in each computational cell is therefore determined by the tolerance to which the Poisson equation is converged. This has implications for discrete energy conservation. Summation of Eq. (29) over all volumes yields

$$\sum_{\text{volumes}} V_{cv} \frac{d\phi_{cv}^2}{dt} + \sum_{\text{boundary faces}} \phi_{cv} \phi_{nbr} v_n A_f = - \sum_{\text{volumes}} \phi_{cv}^2 \sum_{\text{faces of cv}} v_n A_f. \tag{32}$$

Note that even if the discrete divergence in each cell may be small, the collective contribution when summed over all volumes can be significant. For example, if $\sum_{\text{faces of cv}} v_n A_f = O(10^{-6})$ in each cell, summation over a million volumes can make the right-hand side of Eq. (32) approach $O(1)$. This cumulative effect can be avoided if $\sum_{\text{faces of cv}} v_n A_f$ is assumed to be 0 when advancing ϕ_{cv} ; i.e.,

$$V_{cv} \frac{d\phi_{cv}}{dt} + \sum_{\text{faces of cv}} \frac{\phi_{nbr}}{2} v_n A_f = 0 \tag{33}$$

is used to advance ϕ_{cv} instead of Eqs. (26) and (27).

This observation is extended to the Navier–Stokes equations by computing the convection term in a similar manner. In particular, for $\phi = u_i$ this result indicates that the only net convection of kinetic energy fluxes occurs through the boundary, or in other words there is no production of kinetic energy in the computational domain due to the numerics in the absence of time-discretization errors.

A predictor–corrector formulation is derived that emphasizes energy conservation for the convection and pressure terms on arbitrary grids. Accordingly, the cell velocities u_i and the face-normal velocities v_n defined at the center of the face are treated as essentially independent variables. This storage of variables is similar to that used by Rhie and Chow [32] but as will be seen below, the details of the discretization are quite different. Specifically, it will be seen that we do not add a contribution proportional to the difference between the pressure gradient at the center of the cells and the pressure gradient at the center of the faces as advocated by Rhie and Chow [32].

A predictor–corrector formulation is used along with explicit time-advancement.

$$\frac{\hat{u}_i - u_i^k}{\Delta t} = \frac{1}{2}[3(\text{NL} + \text{VISC})^k - (\text{NL} + \text{VISC})^{k-1}], \tag{34}$$

where NL and VISC denote the nonlinear and viscous terms, respectively. The predicted values of u_i are used to obtain predicted values for the face-normal velocities,

$$\hat{v} = \left(\frac{\hat{u}_i^{\text{icv1}} + \hat{u}_i^{\text{icv2}}}{2} \right) n_i, \tag{35}$$

where the face-normal, \vec{n} and therefore \hat{v} point from the volume, icv1 to icv2. The predicted face-normal velocities are projected using

$$\frac{v_n - \hat{v}}{\Delta t} = - \frac{\partial p}{\partial n}. \tag{36}$$

The divergence-free constraint requires that

$$\sum_{\text{faces of cv}} v_N A_f = 0 \Rightarrow \Delta t \sum_{\text{faces of cv}} \frac{\partial p}{\partial N} A_f = \sum_{\text{faces of cv}} \hat{v} A_f. \quad (37)$$

The subscript “N” is used to denote the direction along the face-normal in the outward direction for the control volume under consideration. The above Poisson equation (in integral form) is solved iteratively. Once p is obtained, the Cartesian velocities are updated as

$$\frac{u_i^{k+1} - \hat{u}_i}{\Delta t} = -\frac{\partial p}{\partial x_i}. \quad (38)$$

It turns out that the details of how $\partial p / \partial x_i$ are computed affect the robustness of the solution on highly skewed grids. An obvious approach to computing the gradient at cell centers is to use the gradient theorem:

$$\frac{\partial p}{\partial x_i} = \frac{1}{V} \sum_{\text{faces}} p_{\text{face}} A_f N_i. \quad (39)$$

When applied to flows such as homogeneous turbulence (Section 3.2.2) or the coaxial combustor (Section 3.2.4) for which the grids are fairly regular, very accurate results are obtained. However when applied on the highly skewed grids encountered in a gas-turbine combustor geometry (Section 3.3), unstable solutions were obtained. This behavior was found at both high and low Reynolds numbers, pointing to the pressure gradient as the source of the problem. This lack of robustness can be understood from the contribution of the pressure gradient to the discrete kinetic energy equation. It can be shown that the pressure-gradient term in a fully staggered approach is discretely energy conserving; however, that is not the case in the algorithm described above.

Consider the contribution of the pressure-gradient term to the kinetic energy in a fully staggered formulation. The pressure-gradient term appears as

$$\frac{\partial v_n}{\partial t} = -\frac{\partial p}{\partial n} + \dots \quad (40)$$

Since v_n points from volume icv1 to icv2,

$$\frac{\partial v_n}{\partial t} = -\frac{p_{\text{icv2}} - p_{\text{icv1}}}{d_f}, \quad (41)$$

where d_f denotes the normal distance between the centroids of the two volumes on either side of the face. This implies that

$$v_n \frac{\partial v_n}{\partial t} A_f d_f = -v_n (p_{\text{icv2}} - p_{\text{icv1}}) A_f. \quad (42)$$

Summation over all faces in the domain yields,

$$\sum_{\text{faces}} \frac{\partial}{\partial t} \left(\frac{v_n^2}{2} A_f d_f \right) = - \sum_{\text{faces}} v_n (p_{\text{icv2}} - p_{\text{icv1}}) A_f \quad (43)$$

which is equal to

$$- \sum_{\text{interior faces}} v_n (p_{\text{icv2}} - p_{\text{icv1}}) A_f - \sum_{\text{boundary faces}} v_n (p_{\text{icv2}} - p_{\text{icv1}}) A_f. \quad (44)$$

Adopting the convention that n points out of the domain at the boundary faces, it is readily seen that the above summation reduces to

$$\sum_{\text{faces}} \frac{\partial}{\partial t} \left(\frac{v_n^2}{2} A_f d_f \right) = \sum_{\text{volumes}} p_{\text{icv}} \underbrace{\sum_{\text{faces of cv}} v_N A_f}_0 - \sum_{\text{boundary faces}} v_n p_f A_f, \tag{45}$$

i.e., the contribution of the pressure-gradient to discrete kinetic energy is conservative in a fully staggered formulation. The same is not true in a non-staggered formulation where u_i is computed as

$$\frac{u_i - \hat{u}_i}{\Delta t} = -\frac{1}{V_{\text{cv}}} \sum_{\text{faces of cv}} \frac{(p_{\text{icv}} + p_{\text{nbr}})}{2} N_i A_f. \tag{46}$$

This can be seen as follows. Eq. (46) implies that the pressure gradient contributes to the energy equation as

$$\sum_{\text{volumes}} u_i \frac{\partial p}{\partial x_i} V_{\text{cv}} = \sum_{\text{volumes}} \sum_{\text{faces of cv}} \frac{(p_{\text{icv}} + p_{\text{nbr}})}{2} u_i N_i A_f, \tag{47}$$

which is equal to

$$\sum_{\text{volumes}} \sum_{\text{faces of cv}} (p_{\text{icv}} + p_{\text{nbr}}) v_N A_f, \tag{48}$$

which may be expressed as

$$\sum_{\text{volumes}} p_{\text{icv}} \underbrace{\sum_{\text{faces of cv}} v_N A_f}_0 + \sum_{\text{volumes}} \sum_{\text{faces of cv}} p_{\text{nbr}} v_N A_f, \tag{49}$$

which is not expressible solely in terms of contributions from the boundary faces. The pressure-gradient term is therefore not conservative, in terms of its contribution to the kinetic energy. The main reason for this is that the projected face-normal velocities

$$v_n \neq \left(\frac{u_i^{\text{icv1}} + u_i^{\text{icv2}}}{2} \right) n_i. \tag{50}$$

The following procedure was therefore derived for the pressure-gradient in advancing the Cartesian velocities at the centers of the volumes. Eq. (46) implies that

$$(u_i^{\text{icv1}} + u_i^{\text{icv2}}) n_i - (\hat{u}_i^{\text{icv1}} + \hat{u}_i^{\text{icv2}}) n_i = -\Delta t \left(\frac{\partial p^{\text{icv1}}}{\partial x_i} + \frac{\partial p^{\text{icv2}}}{\partial x_i} \right) n_i. \tag{51}$$

Summing over the faces of each control volume and invoking the projection step (Eq. (36)) yields

$$\sum_{\text{faces of cv}} N_i \left(\frac{u_i^{\text{icv}} + u_i^{\text{nbr}}}{2} \right) A_f - \Delta t \sum_{\text{faces of cv}} \frac{\partial p}{\partial N} A_f = -\frac{\Delta t}{2} \sum_{\text{faces of cv}} \left(\frac{\partial p^{\text{icv}}}{\partial x_i} + \frac{\partial p^{\text{nbr}}}{\partial x_i} \right) N_i A_f. \tag{52}$$

We would like

$$\sum_{\text{faces of cv}} N_i \left(\frac{u_i^{\text{icv}} + u_i^{\text{nbr}}}{2} \right) A_f \tag{53}$$

to be as small as possible. This is possible if $\frac{1}{2} \left(\frac{\partial p^{\text{icv}}}{\partial x_i} + \frac{\partial p^{\text{nbr}}}{\partial x_i} \right) N_i$ across each face is as close to $\partial p / \partial n$ as possible. Since $\partial p / \partial x_i$ is located at the volumes, while $\partial p / \partial n$ is located at the faces, this relation cannot be imposed

exactly. Our approach to make the pressure-gradient term be as energy-conserving as possible is to satisfy this relation in a least-squares sense; i.e., by minimizing

$$\sum_{\text{faces of cv}} \left(\frac{\partial p}{\partial x_i} \Big|_{\text{icv}} n_i^{\text{face}} - \frac{\partial p}{\partial n} \Big|_{\text{face}} \right) A_f. \quad (54)$$

This minimization allows $\partial p / \partial x_i$ to be computed in terms of the nearest neighbors, and is a local operation. The subsequent sections show validation examples of the above formulation. Note that discretizing the convective terms as described above were imperative to obtain robust accurate solutions at high Reynolds numbers. Also one of the simulation examples shown is the exceedingly complicated flow in a gas-turbine combustor. The geometrical complexity made it impossible to avoid the presence of skewed elements. The above least-squares formulation was found imperative to obtain robust, accurate solutions; unstable solutions were obtained in its absence.

3.1. The subgrid model

The dynamic Smagorinsky model [5,21] was extended to unstructured grids, and used for all LES calculations reported in this paper. Note that the Smagorinsky model assumes that

$$q_{ij} = -2C\bar{\Delta}^2 |\bar{S}| \bar{S}_{ij}, \quad (55)$$

where q_{ij} denotes the anisotropic part of the subgrid-scale stress ($\overline{u_i u_j} - \bar{u}_i \bar{u}_j$), $\bar{\Delta}$ denotes the grid-filter width, and \bar{S}_{ij} denotes the filtered strain-rate tensor. Application of the dynamic procedure using the least - squares approach [15] yields the following expression for C :

$$C\bar{\Delta}^2 = -\frac{1}{2} \frac{L_{ij} M_{ij}}{M_{kl} M_{kl}}, \quad (56)$$

where

$$L_{ij} = \widehat{\overline{u_i u_j}} - \widehat{\bar{u}_i} \widehat{\bar{u}_j}, \quad (57)$$

and

$$M_{ij} = \left(\widehat{\bar{\Delta}} / \bar{\Delta} \right)^2 |\widehat{\bar{S}}| \widehat{\bar{S}}_{ij} - |\bar{S}| \bar{S}_{ij}. \quad (58)$$

The dynamic procedure requires definition of a test-filter (denoted by $\widehat{}$), and the ratio of test to grid filter widths ($\widehat{\bar{\Delta}} / \bar{\Delta}$). The ratio of filter widths is assumed to be 2, as is common. The filter width is defined as $V^{1/3}$ where V denotes the element volume. This yields a filter width of $(\Delta_x \Delta_y \Delta_z)^{1/3}$ for a Cartesian grid. The test filter is assumed to be a top – hat filter which uses information from the neighboring volumes.

3.2. Validation

3.2.1. Taylor problem

The importance of discrete energy conservation is illustrated in Fig. 9, which shows the evolution of kinetic energy in the Taylor problem Eq. (16). Our non-staggered formulation (Section 3) is compared to another non-dissipative formulation that only conserves momentum (central differences are applied to the divergence form of the convective term). Both formulations have the same computational stencil, are applied on the same uniform computational grid, and are time-advanced using the same time-step ($0.0002\lambda/u_{\max}$ where λ and u_{\max} denote the wavelength, and maximum initial velocity of a single vortex

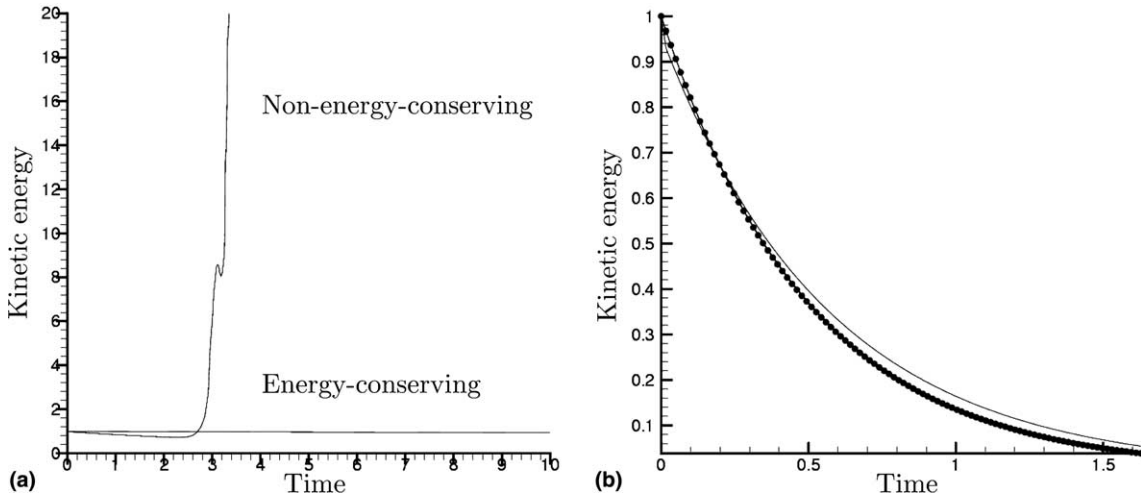


Fig. 9. Illustration of the importance of discretely conserving kinetic energy. The kinetic energy is plotted against time for the Taylor problem at: (a) $Re = 10^9$, and (b) $Re = 1$. At the lower Reynolds number, both schemes are stable. At higher Reynolds number, only the energy-conserving scheme is stable. The solid circles in (b) denote the analytical solution; the energy-conserving formulation passes through them.

pair). No subgrid model is used in these computations. At low Reynolds numbers, where the dissipative scales are resolved, both formulations are stable, although the energy conserving formulation shows better agreement with the analytical result. However, at very high Reynolds numbers where the dissipative scales are not resolved, the formulation that does not conserve kinetic energy becomes unstable after some time, while the energy conserving formulation is seen to maintain its initial kinetic energy as required by the analytical solution. These results may be interpreted more generally. If the computational grid is fine enough that viscous dissipation (the peak of the dissipation spectrum) is resolved on the grid, then discrete energy conservation is not essential; higher order of accuracy might be preferable. On the other hand, if the grid is not fine enough to resolve viscous dissipation, then discrete energy-conservation is essential to obtain stable, accurate solutions. By definition, LES does not resolve viscous dissipation on the computational grid, hence the importance of discrete energy conservation. It can be argued that the subgrid model provides dissipation which can stabilize the LES solution. In our experience, this does not usually happen at high Reynolds numbers in complex geometries. The primary reason for this is that the subgrid model will stabilize the solution only if it removes energy at the same or greater rate than that at which the energy cascades down to the smallest resolved scales. There is no assurance of this happening in general.

3.2.2. Decay of isotropic turbulence

The subgrid term in the LES equations models the transfer of kinetic energy between the resolved scales and the unresolved scales. Non-dissipative numerics make two things possible – the solution exhibits the proper Reynolds number sensitivity, and since the computations are stable without being dissipative, the subgrid model can be turned off, and its contribution to the LES solution assessed.

Fig. 10 illustrates this behavior. The decay of turbulent kinetic energy of isotropic turbulence when computed on a very coarse uniform grid (16^3) is shown. The Reynolds number is increased from 100 to 10^9 while keeping the grid fixed. Computations without a subgrid model are contrasted to those with a subgrid model. Even the lowest Reynolds number computation is not completely resolved at this resolution. Note that in the absence of the subgrid model, the solution does not become numerically unstable; instead it exhibits the proper Reynolds number sensitivity (reduced decay rate with increasing Reynolds number).

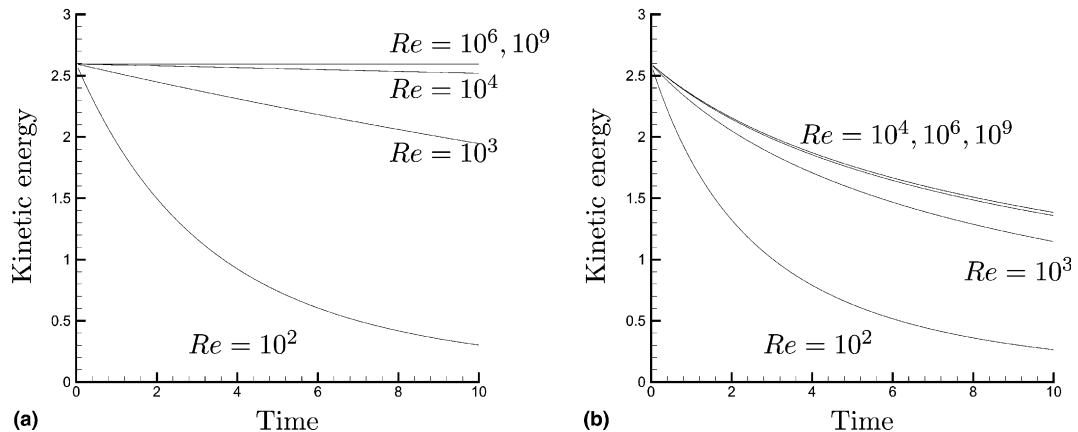


Fig. 10. Resolved kinetic energy of isotropic turbulence is plotted against time at various Reynolds numbers. (a) without subgrid model. (b) with subgrid model.

The decay rate is seen to increase in the presence of the subgrid model, and for $Re > 10^4$, the rate of decay becomes nearly independent of Reynolds number. This trend is physically correct, since increasing the Reynolds number while keeping the grid fixed moves viscous dissipation to smaller and smaller scales. Beyond a certain Reynolds number most of the viscous dissipation occurs outside the range of scales resolved by the grid. At this point, the energetics of the resolved scales are determined only by the transfer of energy to the unresolved scales; i.e., the eddy viscosity of the subgrid model far exceeds physical viscosity, and no further dependence of Reynolds number is observed. Note that in contrast, if the underlying numerical scheme were dissipative then the kinetic energy would decay at a rate determined by the numerical scheme and not the subgrid model.

3.2.3. Flow over a circular cylinder

The flow over a circular cylinder is chosen as a validation example for external flow. Cylinder flow varies significantly with Reynolds number, and is therefore a challenging candidate for validation. Also, experimental data and results from past computations on structured grids are available. DNS was performed at cylinder Reynolds numbers of 20, 100 and 300, and LES was performed at a Reynolds number of 3900. Note that the solution is two-dimensional and steady at $Re = 20$, two-dimensional and unsteady at $Re = 100$, three-dimensional and unsteady at $Re = 300$, and turbulent at $Re = 3900$.

Only the $Re = 300$ DNS and $Re = 3900$ LES are shown here in the interest of brevity. Results for the lower Reynolds numbers are described by [18] where they are shown to agree very well with past experiments and computations. Relevant details of the grids used for the higher Reynolds numbers follow. An unstructured grid of quadrilaterals was first generated in a plane, such that nodes were clustered in the boundary layer and the wake. This two-dimensional grid was then extruded in the spanwise direction to generate the three-dimensional grid; 32 planes were used for the $Re = 300$ and 3900 simulations and periodic boundary conditions imposed in those directions. Uniform flow was specified at the inflow, and convective boundary conditions were enforced at the outflow.

The $Re = 300$ computations were performed on a domain whose inflow and outflow planes were $22D$ from the center of the cylinder (D denotes the cylinder diameter). The domain height was $40D$ and spanwise extent πD . The grid had a total of 1.2 million hexahedral control volumes. The smallest elements immediately adjacent to the cylinder, were of size $2.2e^{-3}D$ radially and $0.01D$ in the azimuthal direction. The wake was resolved using elements of size varying from $0.2D \times 0.07D$ to $2D \times 2D$ in the far-field. The domain for the $Re = 3900$ computations extended $30D$ upstream and $35D$ downstream of the center of the

cylinder. The domain height was $50D$ and spanwise extent was πD . The smallest elements in the boundary layer were $2.5e^{-3}D$ radially and $0.012D$ in the azimuthal direction. Note that this resolution is approximately the same as that used in the $Re = 300$ DNS. The elements are approximately $0.04D \times 0.04D$ for a distance of $1.5D$ in the wake, outside of which they increase from $0.7D \times 0.1D$ in the near-field to $0.8D \times 1.1D$ in the far-field. Fig. 11 shows the grids used for both computations. Statistics were computed by averaging over time and the spanwise direction. The $Re = 300$ simulations used a time-step of $0.016D/U_{\text{freestream}}$ for a total time of $240D/U_{\text{freestream}}$. 90 time units were used to allow initial transients to exit the domain, and statistics were collected over the remaining 150 time units. The $Re = 3900$ simulations used a time-step of $0.001D/U_{\text{freestream}}$ for a total time of $230D/U_{\text{freestream}}$. 80 time units were used to allow initial transients to exit the domain, and statistics were collected over the remaining 150 time units.

The $Re = 300$ results are compared in Fig. 12 to B-spline-Fourier computations by [13], and the spectral computations of [23] and good agreement is observed. Figs. 13 and 14, and Table 2 show results from the $Re = 3900$ LES. Global variables such as recirculation length, Strouhal number, separation point, and profiles of the mean velocities and turbulent Reynolds stresses are seen to be in good agreement with experiments [16,30] and past computations [12,24].

3.2.4. Flow in a coaxial combustor

The flow in a coaxial combustor is chosen as a sample internal flow, due to the presence of multiple streams, swirl and separation. Results are shown for incompressible turbulent flow in a coaxial combustor configuration at conditions corresponding to experiments by [33]. Note that the algorithm described in this paper has been extended to variable density, reacting flow and reacting simulations performed in the same geometry [20]. The domain consists of a central core (primary) and annular (secondary) jets discharging into a cylindrical test section with sudden expansion. The primary jet has a radius of 16 mm and the secondary annular jet extends over the radial interval of 19–32 mm. The outer radius of the annulus is 32 mm, the test-section is 960 mm long, and flow in the annular section has mean swirl. The Reynolds number of the primary jet is 26,200 and the swirl number (ratio of mean azimuthal to axial momentum) in the annulus is 0.47. The ratio of flow rates of the annular jet to the primary jet is 3.87.

The computational domain is divided into $\sim 1.6 \times 10^6$ hexahedral volumes, with $\sim 0.9 \times 10^6$ elements clustered in the first half of the test section. The smallest grid spacing is $\sim 32 \mu\text{m}$ near the walls and in the shear layers close to the annular inlet into the test section. Unsteady velocities corresponding to turbulent

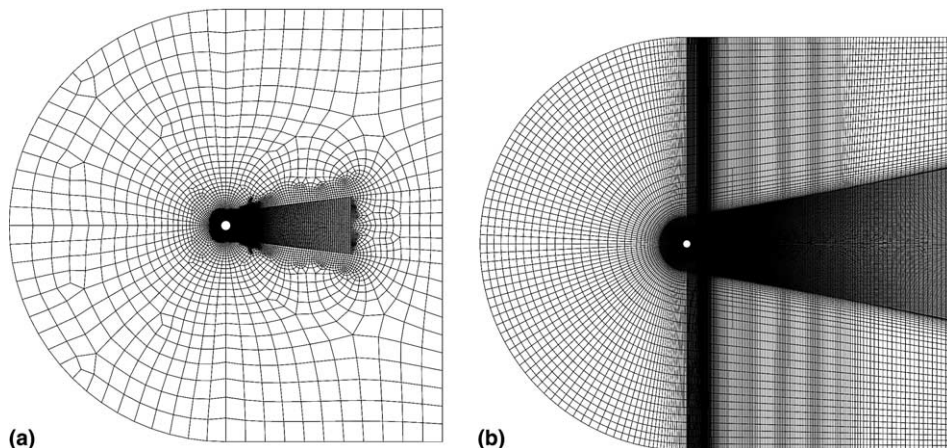


Fig. 11. Cross-section of the grids used in the circular cylinder simulations. (a) $Re = 300$. (b) $Re = 3900$.

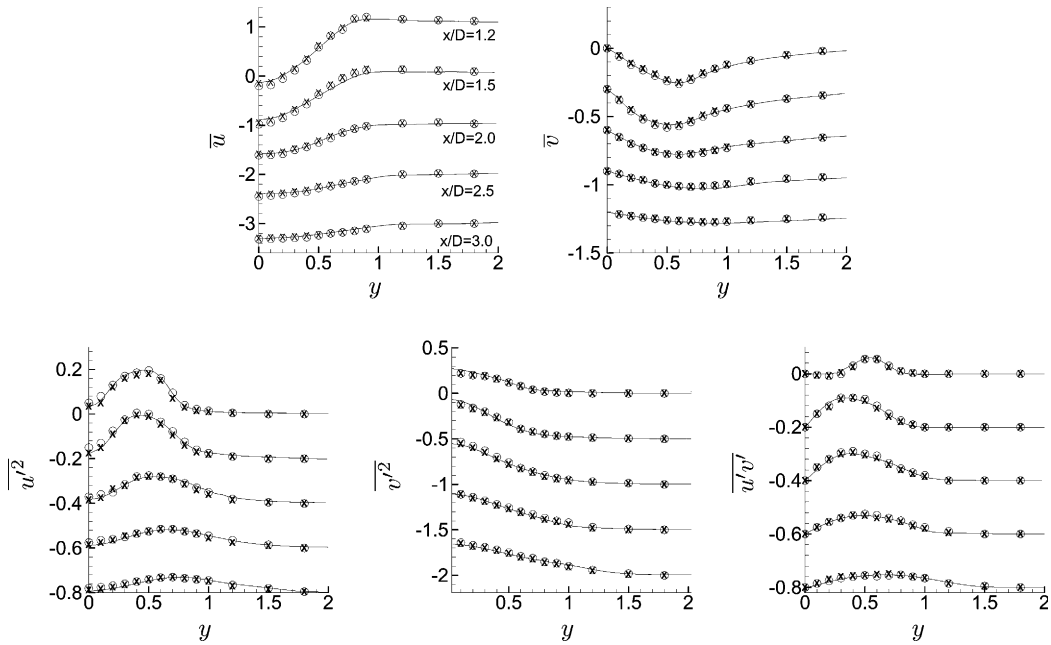


Fig. 12. Vertical profiles at streamwise stations behind the cylinder at $Re = 300$. The unstructured solutions (—) are compared to the B-spline Fourier simulations of Kravchenko et al. [13] (○) and spectral simulations of Mittal and Balachandar [23] (×). The overbars denote averages over time and the span, and primes denote fluctuations about the average.

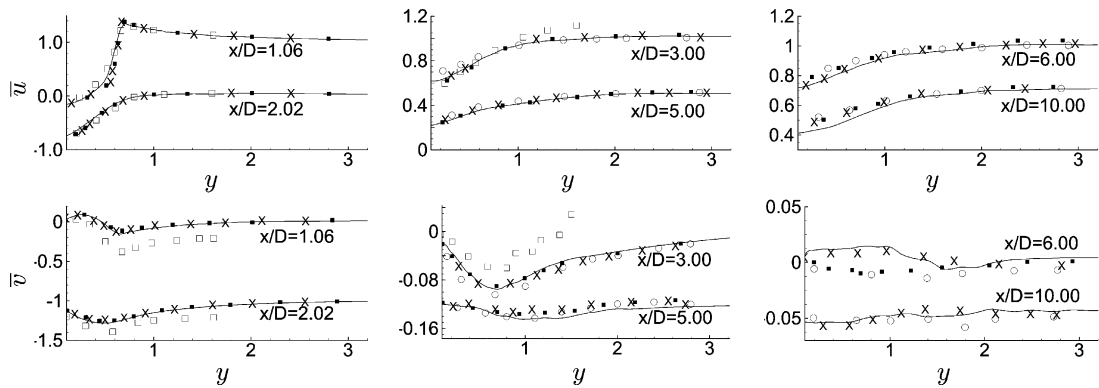


Fig. 13. Vertical profiles of mean velocity at streamwise stations behind a cylinder at $Re = 3900$. The unstructured solutions (—) are compared to Mittal and Moin [24] (×), Kravchenko and Moin [12] (■), Lourenco and Shih [16] (□) and Ong and Wallace [30] (○).

pipe flow, and turbulent annular swirling flow, from a separate computation were specified at the inflow. Convective boundary conditions were imposed at the outflow. The simulations used a time-step of $0.01D_{\text{primary jet}}/U_{\text{primary jet}}$ for a total of 180 time units. Sixty time units were used to allow initial transients to exit the domain, and statistics were collected over the remaining 120 time units. Fig. 15 shows computed contours of streamwise velocity. The divergence of the annular flow, establishment of central recirculation region, and the range of scales of motion are apparent. Profiles at six stations of mean streamwise, radial

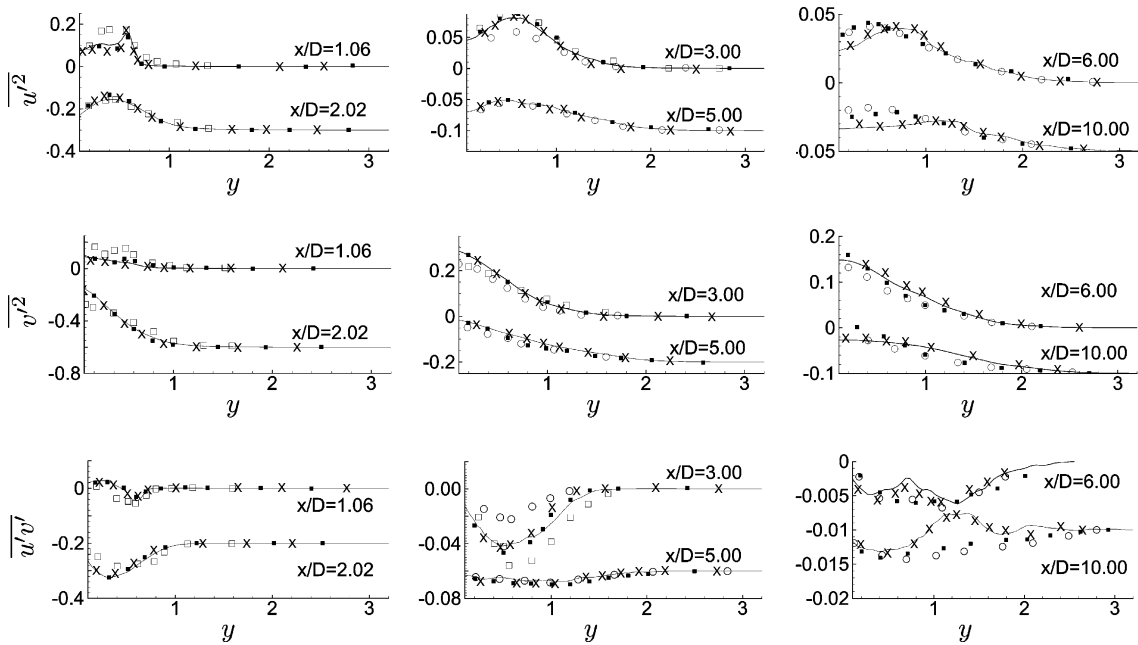


Fig. 14. Vertical profiles of turbulence intensities at streamwise stations behind the cylinder at $Re = 3900$. The unstructured solutions (—) are compared to Mittal and Moin [24] (×), Kravchenko and Moin [12] (■), Lourenco and Shih [16] (□) and Ong and Wallace [30] (○).

Table 2

Comparison of results from LES of the flow around a circular cylinder at $Re = 3900$ to past experiments and computations

	Grid (10^6 cvs)	C_d	St	U_{min}	$\theta_{sep.}$ (°)	L_{rec}/D
Lourenco and Shih (expt.) [16]		0.99	0.215	-0.24	86.0	1.40
Mittal and Moin (LES) [24]	2.3	1.00	0.207	-0.35	86.9	1.40
Kravchenko and Moin (LES) [12]	1.3	1.04	0.210	-0.37	88.0	1.35
Present	1.5	1.00	0.218	-0.31	87.6	1.35

C_d , St , U_{min} , $\theta_{sep.}$, and L_{rec} denote the drag coefficient, Strouhal number, minimum mean streamwise velocity in the recirculation region, separation angle, and length of the recirculation region, respectively.

and azimuthal velocities and turbulence kinetic energy are compared to experiment in Fig. 16, and good agreement is observed.

3.3. Pratt and Whitney gas turbine combustor

Incompressible simulations were performed in the exceedingly complex geometry of a combustor corresponding to a Pratt and Whitney gas-turbine engine. Note that the algorithm described in this paper has been extended to variable density, reacting flow and preliminary reacting simulations performed in the same geometry [7,19]. Fig. 17 shows the level of geometrical complexity; the combustor has numerous passages, holes of various sizes and shapes, swirlers, and obstacles in the flow path. The combustor chamber is fed by three coaxial swirlers and several dilution holes. The inlet air passes through the pre-diffuser and follows

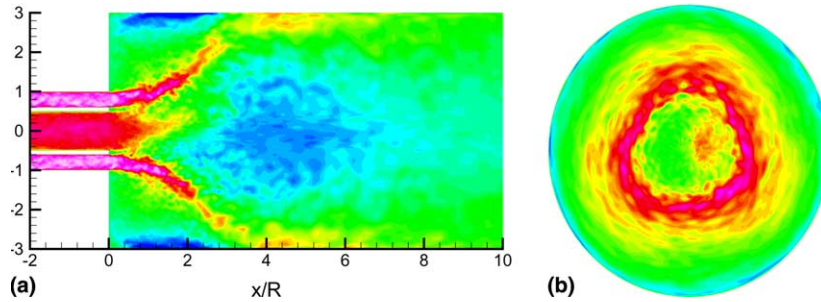


Fig. 15. Contours of axial velocity in LES of incompressible swirling flow in a coaxial combustor geometry. Only part of the computational domain is shown for clarity. (a) $z = 0$ plane, (b) $x = 1.63D$ plane.

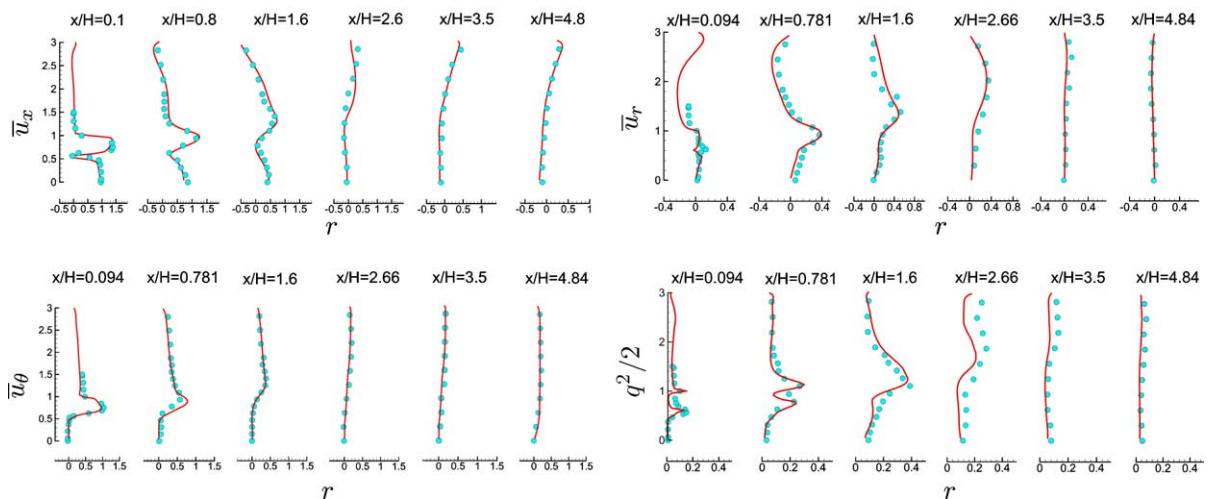


Fig. 16. Profiles of mean velocity and turbulent kinetic energy in LES of incompressible swirling flow in a coaxial combustor geometry. The lines are results from the LES, and symbols are experimental data from [33].

two paths; the main stream flows through the swirlers and enters the chamber, while the secondary stream is diverted to the outer diffusers, and enters the combustor through the dilution holes. The computational domain was divided in ≈ 100 volumes for grid-generation; hexahedral meshes were generated over $\approx 85\%$ of the volumes. Tetrahedral meshes were generated for the swirlers, and pyramids were used to connect tetrahedral and hexahedral elements.

Results are shown for a grid of ≈ 1.3 million elements (0.6 million tetrahedra, 0.65 million hexahedra). Note that the grid consists of highly skewed elements with rapid variations in element size and type. Proprietary experimental data for mass-flow splits and mean pressure-drops was used for validation. Even on this fairly coarse grid, the pressure drops and mass flow through different components were predicted to within 5%. The Reynolds number in the pre-diffuser based on the bulk velocity and cross-section was 500,000; that in the main (core) swirler channel was 150,000. Turbulent fluctuations from a separate calculation in a pipe sector of identical shape as the pre-diffuser inlet section were specified at the inlet. The simulations used a time-step of $0.0067D_{\text{inflow}}/U_{\text{inflow}}$ for a total of 150 time units. Note that D_{inflow} denotes

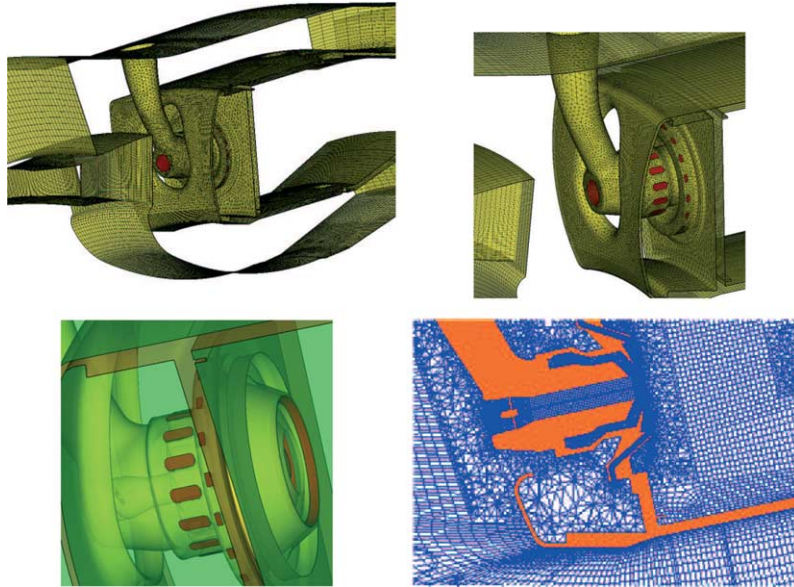


Fig. 17. Illustration of the geometry and surface mesh in the Pratt and Whitney combustor.

the height of the pre-diffuser at the inflow. 70 time units were used to allow initial transients to exit the domain, and statistics were collected over the remaining 80 time units.

Fig. 18 shows the very complex flow pattern inside the main combustion chamber due to the interactions among the swirling jets exiting the injector and the jets entering the combustion chamber through the inner and outer dilution holes. Table 3 compares LES predictions of the mass flow through various components to experiment; good agreement is observed. Fig. 19 defines the various components. Note that ‘OD’ and ‘ID’ in Table 3 refer to the outer diffuser and inner diffuser, respectively. Also, both columns in Table 3 show LES error. The second column shows the error as a percentage of its experimental value in the component, while the third column shows the error as a percentage of the mass flow at the inlet.

Section 3.2.2 noted that the present algorithm displays the proper Reynolds number sensitivity over a range of Reynolds numbers, both with, and without a subgrid model. This observation was made using homogeneous, isotropic turbulence. Fig. 19 draws the same conclusion in the exceedingly complicated

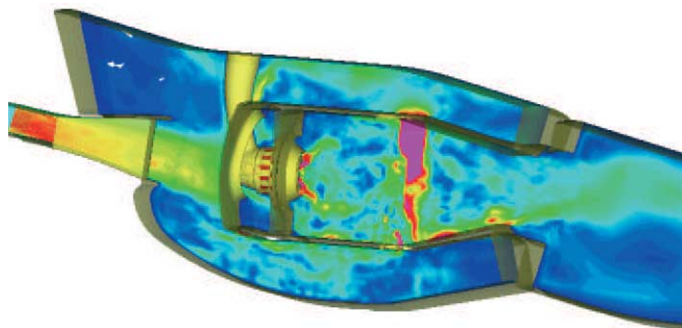


Fig. 18. Contours of instantaneous velocity magnitude in the Pratt and Whitney combustor geometry.

Table 3
Comparison to experiment of mass-flow splits in the Pratt and Whitney combustor

Location	LES Error % wrt expt.	LES Error % wrt inlet
OD dilution hole	3.1	0.8
ID dilution hole	3.5	0.5
Core swirler	10.3	0.14
Second swirler	7.5	0.35
Third swirler	0.4	0.02

'OD' and 'ID' refer to the outer diffuser and inner diffuser, respectively.

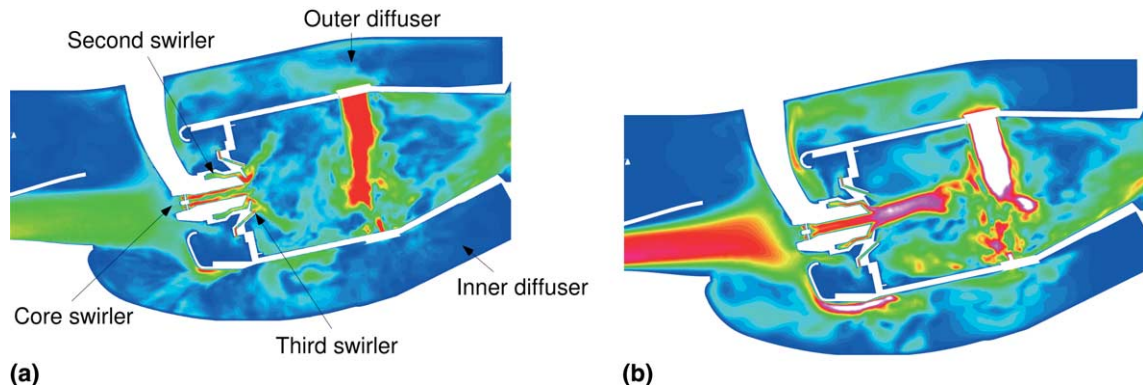


Fig. 19. Contours of instantaneous velocity magnitude in the Pratt and Whitney combustor geometry. (a) high Reynolds number, (b) low Reynolds number.

combustor geometry. The figures show contour plots of the velocity magnitude in the central plane. The computational grid is the same for both plots; the only difference is that the Reynolds number in figure (b) is a factor of 100 lower than that in figure (a). The qualitative difference between both solutions is striking. The co-annular streams diverge and set up a recirculation region at high Reynolds numbers. At the lower Reynolds numbers, no divergence is visible; instead the primary stream issues as a simple jet. This behavior can be physically explained. The primary swirlers in the central passage generate swirl which then decays as the fluid proceeds along the passage. At high Reynolds numbers, the swirl decays by negligible amounts so that the jets that enter the combustor chamber have high levels of swirl. At low Reynolds numbers, the decay in swirl is large enough that the jets entering the combustion chamber have negligible levels of swirl, and therefore do not diverge radially. A corollary of these results is that a combination of numerical dissipation and coarse grids in the central passage can similarly cause the swirl to decay. Excessive dissipation can therefore cause solutions to be wrong even qualitatively.

4. Summary

We have discussed the development of a numerical algorithm and solver capable of performing large-eddy simulation (LES) in the very complex geometries often encountered in industrial applications. The algorithm is developed for unstructured hybrid grids, is non-dissipative, yet robust at high Reynolds numbers on highly skewed grids. Simulation results for the Taylor problem, isotropic turbulence, turbulent

flow over a cylinder, flow in a coaxial combustor and the flow in an industrial gas-turbine combustor were discussed. The paper demonstrates the importance of numerical method in large-eddy simulation, and proposes an algorithm that transitions large-eddy simulation from academic problems to complex industrial flows.

Acknowledgements

This work was supported by the United States Department of Energy under the Accelerated Strategic Computing Initiative. We are grateful to Mr. Gianluca Iaccarino for his assistance in generating the grid used in the combustor simulations, and to Dr. Sourabh Apte and Mr. Suman Muppidi for useful discussions. We are thankful to Pratt and Whitney for the combustor geometry, validation data, and valuable technical input during various stages of this work. Computer time was provided by the San Diego Supercomputing Center and the Minnesota Supercomputing Institute.

References

- [1] R. Amit, C.A. Hall, T.A. Porsching, The dual variable method for solving fluid flow difference equations on Delaunay triangulations, *J. Comput. Phys.* 40 (1981) 183.
- [2] A. Arakawa, Computational design for long term numerical integration of the equations of fluid motion: two-dimensional incompressible flow, Part I, *J. Comput. Phys.* 1 (1966) 119–143.
- [3] H. Deconinck, T. Barth, Special course on unstructured grid methods for advection-dominated flows, AGARD Report, 1992, p. 787.
- [4] J.E. Fromm, F.H. Harlow, Numerical solution of the problem of vortex street development, *Phys. Fluids* 6 (1963) 175–182.
- [5] M. Germano, U. Piomelli, P. Moin, W.H. Cabot, A dynamic subgrid-scale eddy viscosity model, *Phys. Fluids A* 3 (7) (1991) 1760–1765.
- [6] U. Ghia, K.N. Ghia, C.T. Shin, High- Re solutions for incompressible flow using the Navier–Stokes equations and a multigrid method, *J. Comput. Phys.* 48 (1982) 387–411.
- [7] F. Ham, S.V. Apte, G. Iaccarino, X. Wu, S. Herrmann, G. Constantinescu, K. Mahesh, P. Moin, Unstructured LES of reacting multiphase flows in realistic gas-turbine combustors, in: *Annual Research Briefs – 2003*, Center for Turbulence Research, Stanford University and NASA-Ames, to appear.
- [8] F.H. Harlow, J.E. Welch, Numerical calculation of time-dependent viscous incompressible flow of fluid with free surface, *Phys. Fluids* 8 (1965) 2182–2189.
- [9] T.J.R. Hughes, L.P. France, G.M. Hulbert, A new finite element formulation for fluid dynamics VIII. the Galerkin/least-squares method for advective–diffusive equations, *Comput. Methods Appl. Mech. Eng.* 73 (1989) 173–189.
- [10] J.M. Hyman, M. Shashkov, The orthogonal decomposition theorems for mimetic finite difference methods, *SIAM J. Numer. Anal.* 36 (3) (1999) 788.
- [11] K.E. Jansen, Large-eddy simulations of flow around a NACA 4412 airfoil using unstructured grids, in: *Annual Research Briefs*, Center for Turbulence Research, Stanford University/NASA Ames Research Center, 1996, pp. 225–232.
- [12] A.G. Kravchenko, P. Moin, Numerical studies of flow over a circular cylinder at $Re_D = 3900$, *Phys. Fluids* 12 (2) (2000) 403–417.
- [13] A.G. Kravchenko, P. Moin, K. Shariff, B-Spline methods and zonal grids for simulations of complex turbulent flows, *J. Comput. Phys.* 151 (1999) 757–789.
- [14] D.K. Lilly, On the computational stability of numerical solutions of time-dependent non-linear geophysical fluid dynamics problems, *Mon. Weather Rev.* 93 (1965) 11–26.
- [15] D.K. Lilly, A proposed modification of the Germano subgrid-scale closure method, *Phys. Fluids A* 4 (3) (1992) 633–635.
- [16] L.M. Lourenco, C. Shih, Characteristics of the the plane turbulent near wake of a circular cylinder – a particle image velocimetry study, private communication, 1993.
- [17] K. Mahesh, G.R. Ruetsch, P. Moin, Towards large-eddy simulation in complex geometries, in: *Annual Research Briefs – 1999*, Center for Turbulence Research, Stanford University and NASA-Ames, 1999, pp. 379–387.
- [18] K. Mahesh, G. Constantinescu, P. Moin, Large-eddy simulation of gas-turbine combustors, in: *Annual Research Briefs – 2000*, Center for Turbulence Research, Stanford University and NASA-Ames, 2000, pp. 219–228.
- [19] K. Mahesh, G. Constantinescu, S. Apte, G. Iaccarino, P. Moin, Large-eddy simulation of gas-turbine combustors, in: *Annual Research Briefs – 2001*, Center for Turbulence Research, Stanford University and NASA-Ames, 2001, pp. 3–17.

- [20] K. Mahesh, G. Constantinescu, S. Apte, G. Iaccarino, F. Ham, P. Moin, Progress towards large-eddy simulation of turbulent reacting and non-reacting flows in complex geometries, in: Annual Research Briefs – 2002, Center for Turbulence Research, Stanford University and NASA-Ames, 2002, pp. 115–142.
- [21] P. Moin, K. Squires, W. Cabot, S. Lee, A dynamic subgrid-scale model for compressible turbulence and scalar transport, *Phys. Fluids A* 3 (1991) 2746–2757.
- [22] N.N. Mansour, P. Moin, W.C. Reynolds, J.H. Ferziger, Improved methods for large-eddy simulation of turbulence, in: F. Durst, B.E. Launder, F.W. Schmidt, J.H. Whitelaw (Eds.), *Proceedings of the Turbulent Shear Flows I*, Springer, Berlin, 1979, pp. 386–401.
- [23] R. Mittal, S. Balachandar, On the inclusion of three dimensional effects in simulations of two-dimensional bluff body wake flows, in: *Proceedings of the ASME Fluids Engineering Division Summer Meeting*, Vancouver, BC, Canada, 1997.
- [24] R. Mittal, P. Moin, Suitability of upwind biased schemes for large-eddy simulation, *AIAA J.* 30 (8) (1997) 1415–1417.
- [25] P. Moin, *Fundamentals of Engineering Numerical Analysis*, Cambridge University Press, 2001.
- [26] P. Moin, J. Kim, On the numerical solution of time-dependent viscous incompressible flows involving solid boundaries, *J. Comput. Phys.* 35 (1980) 381–392.
- [27] P. Moin, K. Mahesh, Direct numerical simulation: a tool in turbulence research, *Ann. Rev. Fluid Mech.* 30 (1998) 539–578.
- [28] R.A. Nicolaides, The covolume approach to computing incompressible flow, in: M.Y. Hussaini, A. Kumar, M.D. Salas (Eds.), *Algorithmic Trends in Computational Fluid Dynamics*, Springer, Berlin/New York, 1993, pp. 295–333.
- [29] R.A. Nicolaides, X. Wu, Covolume solutions of three-dimensional div-curl equations, ICASE Report 95-4, 1995.
- [30] L. Ong, J. Wallace, The velocity field of the turbulent very near wake of a circular cylinder, *Exp. Fluids* 20 (1996) 441–453.
- [31] B. Perot, Conservation properties of unstructured staggered mesh schemes, *J. Comput. Phys.* 175 (2) (2002) 764–791.
- [32] C.M. Rhie, W.L. Chow, A numerical study of the turbulent flow past an isolated airfoil with trailing edge separation, *AIAA J.* 21 (1983) 1525–1532.
- [33] M. Sommerfeld, H.H. Qiu, Detailed measurements in a swirling particulate two-phase flow by a phase-Doppler anemometer, *Int. J. Heat Fluid Flow* 12 (1) (1991) 20–28.
- [34] X. Zhang, D. Schmidt, B. Perot, Accuracy and conservation properties of a three-dimensional unstructured staggered mesh scheme for fluid dynamics, *J. Comput. Phys.* 180 (1) (2002) 183–199.